Journal of Materials Chemistry A

A Novel P3-type Na2/3Mg1/3Mn2/3O2 as High Capacity Sodium-Ion Cathode Using Reversible Oxygen Redox

Journal:	*Journal of Materials Chemistry A*
Manuscript ID	TA-ART-09-2018-009422.R1
Article Type:	Paper
Date Submitted by the Author:	21-Nov-2018
Complete List of Authors:	Song, Bohang; Oak Ridge National Laboratory, Neutron Scattering Division Hu, Enyuan; Brookhaven national lab., ; Brookhaven National Laboratory, Chemistry Department Liu, Jue; Oak Ridge National Laboratory, Chemical and engineering Materials Zhang, Yiman; Oak Ridge National Laboratory Yang, Xiao-Qing; Brookhaven National Lab, Chemistry Nanda, Jagjit; oak ridge national laboratory, Materials Science & Technology Divison Huq, Ashfia; Oak Ridge National Laboratory, Neutron Scattering Division Page, Katharine; Oak Ridge National Laboratory, Chemical and Engineering Materials Division

A Novel P3-type $Na_{2/3}Mg_{1/3}Mn_{2/3}O_2$ as High Capacity Sodium-Ion Cathode Using Reversible Oxygen Redox

Bohang Song,[1] Enyuan Hu,[2] Jue Liu,[1,*] Yiman Zhang,[3] Xiao-Qing Yang,[2] Jagjit Nanda,[3] Ashfia Huq,[1,*] Katharine Page,[1,*]

[1] Neutron Scattering Division, Oak Ridge National Laboratory, Oak Ridge, Tennessee 37831, United States

[2] Chemistry Division, Brookhaven National Laboratory, Upton, New York 11973, United States

[3] Materials Science and Technology Division, Oak Ridge National Laboratory, Oak Ridge, Tennessee 37831, United States

* liuj1@ornl.gov, huqa@ornl.gov, pagekl@ornl.gov

Abstract

There is great interest in the discovery of Li/Na-ion cathode materials with capacity exceeding the limitation of conventional intercalation-based oxide cathodes. One plausible but challenging path is to reversibly use the charge compensation of both lattice oxygen redox and transition metal (*TM*) redox. Here, we report that lattice oxygen redox alone contributes over 190 mAh/g charge capacity (cut-off at 4.65 V vs. Na^+/Na) for the newly synthesized P3-type $Na_{2/3}Mg_{1/3}Mn(IV)_{2/3}O_2$. Similar amounts of discharge capacity are reversibly achieved. The discharge capacity exceeds 220 mAh/g when Mn^{3+}/Mn^{4+} redox is partially used in addition to the oxygen redox reaction. This represents one of the highest energy density sodium-ion cathodes with superior low-cost. Our results reveal that cations with strong ionic bonding nature with oxygen (such as Mg^{2+}) are very effective in inducing the reversible oxygen redox reaction. We also identified the origin of voltage hysteresis to be a P3-to-O3 phase transition in concomitance with Mg^{2+} migration, suggesting further structure engineering that reduces the structure transition induced cation migration is critical for increasing the energy efficiency of the oxygen redox reactions.

Introduction

Charge storage of the conventional intercalation-based Li/Na-ion cathode materials (e.g. $LiCoO_2$ or $LiMn_2O_4$) relies solely on the charge compensation of transition metal (*TM*) redox.[1-4] Thus, the specific capacities of these materials are often limited by the amount of *TM* ions. Additionally, overcharging conventional Li-based layered cathode oxides, such as $LiCoO_2$ or $LiNiO_2$, often leads to the extraction of electrons from the bonded oxygen 2p states and thus leaves holes within these bands. The accumulation of large amounts of electron holes leads to the formation of peroxide ions, which could easily be released as oxygen gas and result in battery failures. This is the conventional view of the intrinsic voltage/capacity limitation of layered cathode materials.[5] Therefore, it has long been believed that oxidizing lattice oxygen ions inevitably leads to the structural breakdown in overcharged layered cathodes.[5] Recently, a class of Li-excess compounds with general formula $Li[Li_xTM_{1-x}]O_2$ ($0 < x < 0.333$) have overturned this conventional assessment.[6-9] It is broadly demonstrated that lattice oxygen redox contributes over half of the total reversible capacity (the exact amount depends on *TM* ions and x values), inciting fierce debate over the underlying mechanism for reversible oxygen redox activity.[10-14] Nevertheless, it is now generally agreed that combining reversible *TM* redox and lattice oxygen redox is one of the most attractive routes to overcoming the intrinsic capacity limitation of the conventional intercalation-based cathodes.[12, 15, 16]

As we approach an economy where electrical storage plays a larger role, there is strong demand to reduce the cost of cathode materials by either replacing Li with Na[3, 17-19] or replacing expensive Co/Ni with earth abundant elements such as Mn or Fe.[20-22] Unfortunately, these strategies often lead to lower charge/discharge potentials and thus decreases the cathode energy density.[5, 22, 23] In contrast to the conventional *TM* redox couples (where the potential varies for different *TM* species), the lattice oxygen redox couple in layered sodium cathodes are universally located around 4.2 V versus Na^+/Na.[24, 25] Thus, very high energy density may be achieved if large amounts of lattice oxygen redox were accessible during prolonged charge/discharge cycles. Recently, a P2-type $Na_{0.67}Mg_{0.28}Mn_{0.72}O_2$ has been reported to work as a promising high capacity cathode for sodium ion batteries.[25, 26] It was found that the major charge compensation comes from the reversible lattice oxygen redox with minor capacity contribution from residual Mn^{3+}/Mn^{4+} redox. Regarding the structural stability upon (de)sodiation of these P2-type cathodes, Bruce *et al.*[27] has shown that Mg substitution in the P2-$Na_{2/3}Mg_xNi_{1/3-x}Mn_{2/3}O_2$ compounds can efficiently suppress the P2-O2 phase transition and thus improve their electrochemical performance. Although the large voltage hysteresis (between initial charge and discharge) leads to relatively low energy efficiency, it unambiguously demonstrates that non-redox cations other than Li^+ can also effectively induce reversible lattice oxygen redox reaction. Moreover, we recently demonstrated that a near flat discharge plateau with relatively small voltage hysteresis can be realized in the P3-type $Na_{0.6}Li_{0.2}Mn_{0.8}O_2$.[24] In general, the packing of oxygen ions in the P2-type layered oxides follow the sequence of AABBAA… while this stacking sequence changes to AABBCCAABB… in the P3-type structure (Figure S1). Different oxygen frameworks (O3, P3 or P2) is likely to induce a variety of local cation coordination environments and different interlayer and intralayer distances, and thus may lead to drastically different electrochemical properties. This inspires us to explore the plausibility of achieving ultrahigh reversible capacity in the unknown P3-type $Na_{2/3}Mg_{1/3}Mn_{2/3}O_2$ using reversible oxygen redox reaction.

Experimental

Synthesis of P3-type $Na_{2/3}Mg_{1/3}Mn_{2/3}O_2$

Stoichiometric amounts of $NaNO_3$ (99.7%, J. T. Baker), $Mg(NO_3)_2{\cdot}6H_2O$ (97.4%, Mallinckrod) and $MnCO_3$ (99.9%, Aldrich) were mixed and hand ground for 30 mins, the mixture was preheated at 500 °C for 12 h in air. The resulting dark orange powder was then reground and pressed into half-inch pellets and further annealed at 600 °C in a box furnace for 24 h.

Electrochemistry

The electrode slurry was first prepared by mixing the as-synthesized $Na_{2/3}Mg_{1/3}Mn_{2/3}O_2$, carbon black (Super P), and polyvinylidene fluoride (PVDF) (8:1:1 in w/w/w) together using N-Methyl-2-pyrrolidone (NMP) solvent. The slurry was then cast onto an aluminum foil before drying it at 120 °C in a vacuum oven overnight. The electrode after punching (~ 1.1 cm in diameter) has a typical loading density of ~ 2-3 mg/cm^2. A Na half-cell was assembled in an Ar-filled glovebox using the as-prepared cathode, Na metal anode, glass fiber separators, and several drops of electrolyte (1 M $NaClO_4$ in a 98: 2 (v/v) propylene carbonate (PC) and fluoroethylene carbonate (FEC) solution). Galvanostatic charge/discharge cycling was conducted using a Maccor test station where 1C equals 150 mA/g. For all the *ex situ* measurements on the cycled electrodes, the cells were first charged/discharged to the different states as required and then held for at least 12 h to reach the equilibrium condition. The cells were then disassembled in an Ar-filled glovebox to collect the cycled powders. No washing was conducted to avoid electrode degradation caused by the trace amount of water in the solvent.

X-ray and neutron diffraction

High-resolution synchrotron XRD data were collected at the beamline 11-BM at Argonne National Laboratory (ANL) with a wavelength of 0.412748 Å.[28] X-ray total scattering data were collected on the beamline 11-ID-B at the APS using an X-ray energy of 58.6 keV (λ = 0.2114 Å).[29] A PerkinElmer amorphous Si two-dimensional image-plate detector (2048 × 2048 pixels and 200 ×

200 mm pixel size) was used for two-dimensional data collection with the sample-to-detector distance of ∼180 mm. The two-dimensional data were converted to one-dimensional XRD data using the GSAS-II software.[30] PDF data were obtained from Fourier transformation of the background and Compton scattering corrected data [S(Q)] in PDFgetX2 with a Q range of 0.2–24 $Å^{-1}$.

Room temperature neutron total scattering data were collected at the NOMAD beamline at the Spallation Neutron Source (SNS) at ORNL.[31] About 0.5 g powder sample was loaded into a 3 mm quartz capillary. Four ~30 min scans were collected for each powder sample and then summed together to improve the statistics. The detectors were calibrated using scattering from a diamond powder standard prior to the measurements. Neutron powder data were normalized against a V rod and the background was subtracted. The total scattering structure factor S(Q) data were then transformed to PDF data $G(r)$ using the specific IDL codes developed for the NOMAD instrument with a Q range of 0.5–30.0 $Å^{-1}$.

Local and average structure refinements using X-ray and neutron diffraction data were carried out in *TOPAS Academic*, *version 6*.[32] For the refinements using PDF data, the instrumental related dampening [dQ, instrumental FWHM of S(Q)][33] and broadening (Q_b)[34] were refined from the PDF data of standard NIST Si (neutron) or Ni (X-ray) powder. dQ and Q_b were refined as 0.054 Å (1−30 Å) and 0.026 $Å^{-2}$ for NOMAD and 0.069 Å (1−30 Å) and 0.025 $Å^{-2}$ for 11-ID-B. These two values were fixed during further structure refinements. A sinc function [sin(Qr)/Qr] was convoluted with the calculated PDF to account for the termination effect due to the finite Q_{max} used for Fourier transformation.[35] The empirical PDFgui-type δ^2 (δ^2/r^2) term was used to model correlated motion effects.[34] For the average structure refinements using synchrotron XRD data, the fundamental parameter approach of diffraction peak profiles was used.[36]

X-ray absorption spectroscopy

X-ray absorption spectroscopy (XAS) measurements were performed at the 8-ID beamline of the National Synchrotron Light Source II (NSLS II) at Brookhaven National Laboratory (BNL) in transmission mode. The X-ray absorption near edge structure (XANES) and Extended X-ray absorption fine structure (EXAFS) spectra were processed using the Athena software package.[37] The AUTOBK code was used to normalize the absorption coefficient, and separate the EXAFS signal, $\chi(k)$, from the isolated atom-absorption background. The extracted EXAFS signal, $\chi(k)$, was weighted by k^2 to emphasize the high-energy oscillations and then Fourier-transformed in a k range from 3.0 to 13.6 $Å^{-1}$ to analyze the data in R space. The Fourier transforms of EXAFS spectrum were fitted in the R range of 1.0~3.0 Å, using single scattering paths generated with the FEFF 6.0 *ab*-initio simulation code.[38] The structure determined from XRD Rietveld refinement was used as a model structure. The amplitude reduction factor (S_0^2) was determined to be 0.59 from the fitting of an MnO_2 standard. The same inner shell potential shift (ΔE) was shared for all the paths fitted. Separate fitting parameters of the bond distance (R) and Debye-Waller factor (σ^2) were used for each shell. The coordination number for all paths are fixed to those in the model structure.

Results and discussion

Crystal structure of P3-type $Na_{2/3}Mg_{1/3}Mn_{2/3}O_2$

Phase pure P3-type $Na_{2/3}Mg_{1/3}Mn_{2/3}O_2$ was for the first time synthesized from a solid-state reaction. The final product is an orange colored fine powder. The major Bragg diffraction peaks of corresponding XRD (λ =0.412748 Å) patterns can be indexed using the P3-type layered structure (S.G. *R*3m), as can be seen in Figure S2. However, it is worth noting the presence of a very broad saw-tooth like diffuse scattering peak at 2θ around 5.5°. This diffuse scattering peak cannot be indexed using the conventional P3-type structure, and it is caused by the in *ab*-plane

Mg^{2+}/Mn^{4+} honeycomb ordering. This cation ordering is further confirmed by the refinement of a honeycomb ordered model using short-range X-ray and neutron PDF data (Figures S3 and S4, Table S2) and Mn K-edge EXAFS data (Figure 4c). The ordering of honeycomb layers along the stacking direction (*c*-axis direction) is limited due to the relatively low annealing temperature, leading to the very asymmetric diffuse scattering peak (or Warren peak), displayed in the inset in Figure 1.[39] Similar features have been observed in other honeycomb ordered layered oxides, such as Li_2MnO_3 and $Na_3Ni_2BiO_6$.[40, 41] Rietveld refinement using Space Group (S.G.) *C*m (maximum subgroup of S.G. *R*3m with monoclinic distortion) leads to a satisfactory fit of the whole pattern. The refined structure is shown in Table 1. It is worth noting that the refined site mixing of Mg and Mn does not indicate actual cation mixing but instead reflects the presence of stacking faults that violates the translation rules along the *c*-axis direction.[41, 42] A detailed analysis of the honeycomb stacking disorder falls outside of the scope of the current paper and will be reported elsewhere.

Electrochemical properties of P3-type $Na_{2/3}Mg_{1/3}Mn_{2/3}O_2$

The Galvanostatic charge and discharge curves of P3-type $Na_{2/3}Mg_{1/3}Mn_{2/3}O_2$ (versus Na^+/Na) are shown in Figure 2a. While the compound suffers performance degradation after initial high capacity charge, its behavior and performance conclusively demonstrates the promotional effects of combining transition metal and oxygen redox mechanisms in a single cathode material. A near flat plateau at approximately 4.2 V can be seen for the initial charge curve, similar to that of the P2-type $Na_{2/3}(Mg_{0.28}Mn_{0.72})O_2$.[25, 26] When the cell was charged to 4.65 V, the specific charge capacity reached 196 mAh/g (Figure S5). It implies all sodium ions are essentially extracted from the lattice (theoretical capacity of 194 mAh/g). Since the discharge capacities with cut-off voltages higher than 4.4 V are very similar, i.e. 222 mAh/g for the 4.4 V cut-off and 230 mAh/g for the 4.65 V cut-off, the 4.4 V cut-off was used to avoid electrolyte decomposition. Since the redox potential of Mn^{4+}/Mn^{5+} is expected to emerge at much higher potentials (>> 4.2 V versus Na^+/Na)[5, 43] and Mg^{2+} is a non-redox cation, this large amount of charge capacity is very likely contributed from the oxidation of lattice oxygen. This is also in good agreement with the well-maintained Mn oxidation state during charge (Figures 4a and 4b).

In contrast to the P3-type $Na_{0.6}Li_{0.2}Mn_{0.8}O_2$,[24] where the initial discharge curve is a flat plateau with very small voltage hysteresis, the discharge curve of the present P3-type $Na_{2/3}Mg_{1/3}Mn_{2/3}O_2$ is a slope-like curve with relatively large voltage hysteresis, similar to that of the P2-type $Na_{0.67}Mg_{0.28}Mn_{0.72}O_2$. This indicates that the stacking sequences of lattice oxygen (e.g. P3 versus P2) is unlikely to be the underlying driving force for the large voltage hysteresis between charge and discharge curves. It is also worth noting that the flat charge plateau can only be partially recovered in the subsequent cycles, as can be seen in Figure 2a and the corresponding dQ/dV plots in Figure 2b, indicating that irreversible structure transition likely occurs after the initial charge. The two redox peaks at 2.06 V (discharge) and ~ 2.17 V (charge) are expected to be associated with the Mn^{3+}/Mn^{4+} redox couple, a conclusion that is fully consistent with the dramatic decrease of the Mn oxidation state after discharging to voltages lower than 2.0 V (Figures 4a and 4b).

The cycling performance for this compound (Figure 2c) is seen to maintain a discharge capacity of 153 mAh/g after 30 cycles at a C/10 rate, though it declines steadily through cycling. The average Coulombic efficiency (CE) reaches 98.4%, excluding the 1st cycle. The dQ/dV plots of the charge/discharge curves upon 30 cycles are shown in Figure 2d. It shows that the capacities contributed from Mn^{3+}/Mn^{4+} and O^{2-}/O^- redox both gradually degrade. Therefore, it is very likely that surface oxygen may release during prolonged cycles, leading to the gradual structural degradation and oxidation of organic electrolyte. Thus, further surface coating or modification is required to improve the cyclability of this compound. The rate capability of $Na_{2/3}Mg_{1/3}Mn_{2/3}O_2$ is moderate, as can be seen in Figures 2e and 2f. This can be ascribed to the presence of large amounts of Mg^{2+} in the *TM* layers, leading to relatively poor electronic conductivity.

Reversible O redox during the 1st cycle

To further confirm the large discharge capacity is mainly from the reversible oxygen redox rather than the Mn^{4+}/Mn^{3+} redox, a controlled charge/discharge experiment as a function of charging time was conducted (Figure 3). The charge capacity continuously increases from 25 to 167 mAh/g as the charging time increases from 5 to 35 h. Most importantly, the discharge capacity above 2 V also increases correspondingly. The cut-off voltage where the discharge capacity exactly matches the charge capacity was recorded for comparison. Surprisingly, these cut-off voltages are within a small region between 2.03 and 2.10 V. A slight difference in the cut-off voltages is due to the various extents of phase transition from the P3 phase to the O3 phase during the initial charging, which will be discussed in a later section. In addition, the dQ/dV plots of the discharge curves show a continuous growth of ~2.7 V peak with increase charging time. These findings unambiguously confirm that the discharge capacity above 2.1 V is mainly from oxygen reduction, in good agreement with the X-ray absorption results (Figure 4a). Mn is tetravalent in the pristine state and charging the sample up to 4.4 V hardly changes its valence, confirming that it is oxygen that contributes to the charge capacity. Upon discharging, Mn only slightly participates in the redox reaction above 2.3 V. The detailed valence change of Mn is shown in Figure 4b, where the valence calculation is based on a previous report.[44] By taking advantage of the FT-EXAFS, the structure of the pristine sample is validated (Figure S6). Particularly, the pattern can be fit well only by considering two different sites for Mg and Mn, confirming the ordering between them. This is consistent with the local structure refined from X-ray/neutron PDF (Figures S3 and S4, Table S2). Figure 4d shows that the Mn-O bond length reversibly decreases upon charging and reversibly increases upon discharging. The same trend also applies to the Mn-Mg/Mn pair distances, indicating shrinking during charging and expansion during discharging. Notably, there is an obvious amplitude reduction upon cycling, suggesting that local structural disorder is likely induced during the process.

Structure origin of voltage hysteresis during the 1st cycle

To further unravel the mechanism of the relatively large voltage hysteresis between the initial charge and discharge, high resolution XRD patterns ($\lambda = 0.412748$ Å) were collected for samples recovered from different charge and discharge states (Figure 5a). A new phase appears in the half-charged sample (charge capacity ~ 85 mAh/g) that cannot be well modeled using the pristine P3-phase (S.G. *R*3m). Instead, it turns out to be the O3-type phase (S.G. *R*-3m). Moreover, the positions of reflections associated with the pristine phase are well maintained, with only the corresponding intensities decreasing during charging, indicating a very limited solid solution region for the P3-type $Na_{2/3-x}Mg_{1/3}Mn_{2/3}O_2$. In contrast, the peak position shifts for the O3 phase at different charge states (e.g. half charged and 4.4 V charged), indicating a relatively wider solid solution range for this phase. This is consistent with the refined sodium occupancy, which decreases from 0.35(1) in the half-charged sample to 0.01(3) in the 4.4 V charged sample. It is also worth noting the continuous peak position shift (to lower 2θ angle) of (003) and (104) reflections for the samples discharged between 4.4 V and 2.1 V (Figure S7). This suggests the structure evolution mainly follows a solid solution path instead of a reversible two-phase reaction (O3 to P3) pathway during the initial discharge, explaining the loss of performance of the cathode in future cycles.

Quantitative phase fractions of the P3 and O3 phases were refined using the Rietveld method and the result is shown in Figure 5b. The refinement results and refined structure are shown in Figure

S8 and Tables S3 to S7. The near linear variation of the fraction of the two phases during initial charge further confirms the nature of the two-phase reaction. About 87% P3 phase is converted to the O3 phase for the sample charged to 4.4 V, in good agreement with the initial charge capacity of ~170 mAh/g. Interestingly, the O3 phase is partially converted to the P3 phase in addition to a pure solid solution reaction when discharged between 4.4 V and 2.75 V (stage I), as evidenced by the increase of intensity of the major 003 (or 001 in monoclinic *C*m indexing, $2\theta \sim 4.2°$) reflection of the P3 phase relative to that of the O3 phase (Figure 5a). This is further confirmed by the decrease of the refined phase fraction of the O3 phase (from ~87% to ~77%). This partial conversion of O3 to P3 phase at voltages higher than 2.75 V explains the partial persistence of the flat charge plateau in subsequent cycles (Figures 2a and 2d). High quality *in situ* diffraction data are required to further quantify the exact voltage region for the O3 to P3 conversion. Nevertheless, the intercalation of sodium (discharge) into the O3 phase predominantly follows a solid solution reaction mechanism, similar to that of various O3-type layered Na_xTMO_2.[45] This explains (from a structure point of view) the near flat plateau for the initial charge curve (two phase reaction) and the slope-like initial discharge curve (solid solution reaction).

Further discharge (from 2.1 V to 1.6 V) results in the partial conversion of the residual P3 phase to the O3 phase, and it also leads to the simultaneous decrease of the interlayer spacing (or *c* lattice parameter) for the O3 phase due to the insertion of Na^+. In contrast, the (101) and (104) reflections shift to the lower 2θ angle, indicating the relatively large expansion in the *ab*-plane. This expansion can be ascribed to the elongation of Mn-O bonds caused by the partial reduction of Mn^{4+}. The utilization of the Mn^{3+}/Mn^{4+} redox couple is further confirmed by the shift of the Mn K-edge XANES to lower energy (Figures 4a and 4b) and the appearance of the redox peak at ~2.0 V in the dQ/dV curve (Figure 2b). The refined sodium occupancy for the sample discharged to 1.6 V is

0.778 (1), which is in good agreement with the initial discharge capacity of ~225 mAh/g. During the 2nd charging process, it is likely that the O3 phase could partially transform back to the P3 phase accompanied with partial Mg migration. Therefore, the remnant P3 phase from the first cycle and the recovered P3 phase from the second cycle together contributes about half of the initial charge capacity at ~ 4.2 V plateau (as can be seen in Figure 2a). The whole cationic ($Mn^{3+/4+}$) and anionic ($O^{2-/-}$) redox are fully reversible in both phases despite the partial transitions between them, leading to the highly reversible discharge capacity for the current system. However, crystallographic structure of the material during the second and the following cycles need to be explored in future.

According to the Rietveld refinement results, the relatively large voltage hysteresis between the initial charge and discharge curves is likely rooted in the following two steps: first, the irreversible transition of lattice oxygen stacking sequences, i.e. from P3 to O3; second, the partial migration of Mg^{2+} from *TM* octahedral sites to the interlayer tetrahedral sites during charge and the counter migration (back to *TM* octahedral sites) during discharge (Figure S9 and Tables S2-S7). It is very likely that the Mg^{2+} migration during charge and counter migration during discharge have dramatically different energy pathways, similar to the cation migration in the Li-excess materials such as $Li[Li_{0.2}Ni_{0.13}Co_{0.13}Mn_{0.54}]O_2$.[46, 47] This synergistic effect results in the very different charge/discharge profiles for the current P3-type $Na_{2/3}Mg_{1/3}Mn_{2/3}O_2$. The schematic summary of the phase transition during the initial charge and discharge is shown in Figure 6. Taken together, it suggests that reducing or eliminating structure transition induced by cation migration is critical for achieving real reversible (both capacity and voltage) oxygen redox reaction for sodium-ion cathodes.

Conclusions

The P3-type $Na_{2/3}Mg_{1/3}Mn_{2/3}O_2$ is found to work as a promising high energy density and superior low-cost sodium-ion cathode using reversible lattice oxygen redox reaction. This discovery highlights that partially replacing *TM* cations with cations exhibiting stronger ionic bonding with oxygen, such as Mg^{2+}, can effectively induce a reversible oxygen redox reaction, paving the way for exploring next generation layered oxide cathodes with low-cost and ultrahigh capacities. The relatively large voltage hysteresis between the initial charge and discharge is rooted in the irreversible P3 to O3 phase transition in concomitance with the partial migration of Mg^{2+}. These findings suggest that further structure engineering that reduces the structure transition induced *TM* layer cation migration is critical for increasing the energy efficiency of oxygen redox reactions.

Conflicts of interest

There are no conflicts to declare.

Supporting information

Le Bail fit of the synchrotron diffraction data of P3-type $Na_{2/3}Mg_{1/3}Mn_{2/3}O_2$ using S.G. *R*3m. Local structure refinements of P3-type $Na_{2/3}Mg_{1/3}Mn_{2/3}O_2$ using X-ray and neutron PDF data. Initial charge and discharge between 1.6 V and 4.65 V. Rietveld refinement results of the O3 and P3 structure of materials at different charge and discharge states.

Acknowledgement

This research is primarily supported by the U.S. Department of Energy, Office of Science, Office of Basic Energy Sciences, Early Career Research Program award KC040602, under contract number DE-AC05-00OR22725. Research conducted at the NOMAD beamline at ORNL's Spallation Neutron Source was sponsored by the Scientific User Facilities Division, Office of Basic Sciences, U.S. Department of Energy. Research at the 11-ID-B and 11-BM beamlines used resources of the Advanced Photon Source, a U.S. Department of Energy (DOE) Office of Science User Facility operated for the DOE Office of Science by Argonne National Laboratory under Contract No. DE-AC02-06CH11357. This research used resources at 7-BM of the National Synchrotron Light Source II, a U.S. Department of Energy (DOE) Office of Science User Facility operated for the DOE Office of Science by Brookhaven National Laboratory under Contract No. DE-SC0012704. Enyuan Hu and Xiao-Qing Yang at Brookhaven National Laboratory were supported by the Assistant Secretary for Energy Efficiency and Renewable Energy, Vehicle Technologies Office of the U.S. DOE through the Advanced Battery Materials Research (BMR)

Program, including Battery500 consortium under Contract DE-SC0012704. We would also like to thank Dr. Nancy Dudney and Dr. Craig Bridges for fruitful discussion and technical review. This manuscript has been authored by UT-Battelle, LLC under Contract No. DE-AC05-00OR22725 with the U.S. Department of Energy. The United States Government retains and the publisher, by accepting the article for publication, acknowledges that the United States Government retains a non-exclusive, paid-up, irrevocable, worldwide license to publish or reproduce the published form of this manuscript, or allow others to do so, for United States Government purposes. The Department of Energy will provide public access to these results of federally sponsored research in accordance with the DOE Public Access Plan (http://energy.gov/downloads/doe-public-access-plan).

References

1 K. Mizushima, P. Jones, P. Wiseman and J. B. Goodenough, *Mater. Res. Bull.*, 1980, **15**, 783-789.

2 M. Thackeray, P. Johnson, L. De Picciotto, P. Bruce and J. Goodenough, *Mater. Res. Bull.*, 1984, **19**, 179-187.

3 N. Yabuuchi, K. Kubota, M. Dahbi and S. Komaba, *Chem. Rev.*, 2014, **114**, 11636-11682.

4 C. Masquelier and L. Croguennec, *Chem. Rev.*, 2013, **113**, 6552-6591.

5 J. B. Goodenough and Y. Kim, *Chem. Mater.*, 2009, **22**, 587-603.

6 Z. Lu, D. MacNeil and J. Dahn, *Electrochem. Solid-State Lett.*, 2001, **4**, A191-A194.

7 M. M. Thackeray, S.-H. Kang, C. S. Johnson, J. T. Vaughey, R. Benedek and S. Hackney, *J. Mater. Chem.*, 2007, **17**, 3112-3125.

8 D. A. Kitchaev, Z. Y. Lun, W. D. Richards, H. W. Ji, R. J. Clement, M. Balasubramanian, D. H. Kwon, K. H. Dai, J. K. Papp, T. Lei, B. D. McCloskey, W. L. Yang, J. Lee and G. Ceder, *Energy Environ. Sci.*, 2018, **11**, 2159-2171.

9 R. A. House, L. Y. Jin, U. Maitra, K. Tsuruta, J. W. Somerville, D. P. Forstermann, F. Massel, L. Duda, M. R. Roberts and P. G. Bruce, *Energy Environ. Sci.*, 2018, **11**, 926-932.

10 K. Luo, M. R. Roberts, N. Guerrini, N. Tapia-Ruiz, R. Hao, F. Massel, D. M. Pickup, S. Ramos, Y.-S. Liu and J. Guo, *J. Am. Chem. Soc.*, 2016, **138**, 11211-11218.

11 K. Luo, M. R. Roberts, R. Hao, N. Guerrini, D. M. Pickup, Y.-S. Liu, K. Edström, J. Guo, A. V. Chadwick and L. C. Duda, *Nat. Chem.*, 2016, **8**, 684.

12 G. Assat and J.-M. Tarascon, *Nat. Energy.*, 2018, **3**, 373-386.

13 E. McCalla, A. M. Abakumov, M. Saubanère, D. Foix, E. J. Berg, G. Rousse, M.-L. Doublet, D. Gonbeau, P. Novák and G. Van Tendeloo, *Science*, 2015, **350**, 1516-1521.

14 D.-H. Seo, J. Lee, A. Urban, R. Malik, S. Kang and G. Ceder, *Nat. Chem.*, 2016, **8**, 692-697.

15 P. Rozier and J. M. Tarascon, *J. Electrochem. Soc.*, 2015, **162**, A2490-A2499.

16 Y. Qiao, S. H. Guo, K. Zhu, P. Liu, X. Li, K. Z. Jiang, C. J. Sun, M. W. Chen and H. S. Zhou, *Energy Environ. Sci.*, 2018, **11**, 299-305.

17 S. W. Kim, D. H. Seo, X. Ma, G. Ceder and K. Kang, *Advanced Energy Materials*, 2012, **2**, 710-721.

18 M. D. Slater, D. Kim, E. Lee and C. S. Johnson, *Adv. Funct. Mater.*, 2013, **23**, 947-958.

19 J. Liu, D. Chang, P. Whitfield, Y. Janssen, X. Yu, Y. Zhou, J. Bai, J. Ko, K.-W. Nam and L. Wu, *Chem. Mater.*, 2014, **26**, 3295-3305.

20 B. Ellis, W. Makahnouk, Y. Makimura, K. Toghill and L. Nazar, *Nat. Mater.*, 2007, **6**, 749-753.

21 N. Yabuuchi, M. Kajiyama, J. Iwatate, H. Nishikawa, S. Hitomi, R. Okuyama, R. Usui, Y. Yamada and S. Komaba, *Nat. Mater.*, 2012, **11**, 512-517.

22 J. Liu, X. Yu, E. Hu, K.-W. Nam, X.-Q. Yang and P. G. Khalifah, *Chem. Mater.*, 2013, **25**, 3929-3931.

23 S. P. Ong, V. L. Chevrier, G. Hautier, A. Jain, C. Moore, S. Kim, X. Ma and G. Ceder, *Energy Environ. Sci.*, 2011, **4**, 3680-3688.

24 X. Rong, J. Liu, E. Hu, Y. Liu, Y. Wang, J. Wu, X. Yu, K. Page, Y.-S. Hu and W. Yang, *Joule*, 2017, **2**, 125-140.

25 U. Maitra, R. A. House, J. W. Somerville, N. Tapia-Ruiz, J. G. Lozano, N. Guerrini, R. Hao, K. Luo, L. Jin and M. A. Pérez-Osorio, *Nat. Chem.*, 2018, **10**, 288-295.

26 N. Yabuuchi, R. Hara, K. Kubota, J. Paulsen, S. Kumakura and S. Komaba, *J. Mater. Chem. A.*, 2014, **2**, 16851-16855.

27 N. Tapia-Ruiz, W. M. Dose, N. Sharma, H. R. Chen, J. Heath, J. W. Somerville, U. Maitra, M. S. Islam and P. G. Bruce, *Energy Environ. Sci.*, 2018, **11**, 1470-1479.

28 J. Wang, B. H. Toby, P. L. Lee, L. Ribaud, S. M. Antao, C. Kurtz, M. Ramanathan, R. B. Von Dreele and M. A. Beno, *Rev. Sci. Instrum.*, 2008, **79**, 085105.

29 P. J. Chupas, X. Qiu, J. C. Hanson, P. L. Lee, C. P. Grey and S. J. Billinge, *J. Appl. Crystallogr.*, 2003, **36**, 1342-1347.

30 B. H. Toby and R. B. Von Dreele, *J. Appl. Crystallogr.*, 2013, **46**, 544-549.

31 J. Neuefeind, M. Feygenson, J. Carruth, R. Hoffmann and K. K. Chipley, *Nuclear Instruments and Methods in Physics Research Section B*, 2012, **287**, 68-75.

32 A. Coelho, P. Chater and A. Kern, *J. Appl. Crystallogr.*, 2015, **48**, 869-875.

33 B. Toby and T. Egami, *Acta Crystallogr. Sect. A: Found. Crystallogr.*, 1992, **48**, 336-346.

34 C. Farrow, P. Juhas, J. Liu, D. Bryndin, E. Božin, J. Bloch, T. Proffen and S. Billinge, *J. Phys.: Condens. Matter*, 2007, **19**, 335219.

35 J. S. Chung and M. Thorpe, *Phys. Rev. B*, 1997, **55**, 1545.

36 R. W. Cheary, A. A. Coelho and J. P. Cline, *Journal of Research of the National Institute of Standards and Technology*, 2004, **109**, 1.

37 B. Ravel and M. Newville, *J. Synchrotron Radiat.,* 2005, **12**, 537-541.

38 M. Newville, *J. Synchrotron Radiat.,* 2001, **8**, 96-100.

39 J. Biscoe and B. Warren, *J. Appl. Phys.*, 1942, **13**, 364-371.

40 J. Bréger, M. Jiang, N. Dupré, Y. S. Meng, Y. Shao-Horn, G. Ceder and C. P. Grey, *J. Solid State Chem.*, 2005, **178**, 2575-2585.

41 J. Liu, L. Yin, L. Wu, J. Bai, S.-M. Bak, X. Yu, Y. Zhu, X.-Q. Yang and P. G. Khalifah, *lnorg. Chem.*, 2016, **55**, 8478-8492.

42 E. M. Seibel, J. Roudebush, H. Wu, Q. Huang, M. N. Ali, H. Ji and R. Cava, *lnorg. Chem.*, 2013, **52**, 13605-13611.

43 K. Du, J. Zhu, G. Hu, H. Gao, Y. Li and J. B. Goodenough, *Energy Environ. Sci.*, 2016, **9**, 2575-2577.

44 E. Y. Hu, X. Q. Yu, R. Q. Lin, X. X. Bi, J. Lu, S.-M. Bak, K.-W. Nam, H. L. Xin, C. Jaye, D. A. Fischer, K. Amine and X.-Q. Yang, *Nat. Energy*, 2018, **3,** 690-698.

45 H. Pan, Y.-S. Hu and L. Chen, *Energy Environ. Sci.*, 2013, **6**, 2338-2360.

46 M. Jiang, B. Key, Y. S. Meng and C. P. Grey, *Chem. Mater.*, 2009, **21**, 2733-2745.

47 F. Dogan, B. R. Long, J. R. Croy, K. G. Gallagher, H. Iddir, J. T. Russell, M. Balasubramanian and B. Key, *J. Am. Chem. Soc.*, 2015, **137**, 2328-2335.

Tables

Table 1 Refined structure of the P3-type $Na_{2/3}Mg_{1/3}Mn_{2/3}O_2$ using synchrotron XRD ($\lambda = 0.412748$ Å)

S.G. *C*m	a = 5.0194(1) Å, b = 8.6888 (8) Å, c = 5.8389(2) Å, β = 106.632(3)°					
Site	Wyck.	x	y	z	Occ.	B_{iso} (Å^2)
Mn1	4b	0.4953(13)	0.1711(2)	0	0.90(1)	0.25(3)
Mg1	4b	0.4953(13)	0.1711(2)	0	0.10(1)	0.10(13)
Mn2	2a	0	0	0	0.20(1)	0.25(3)
Mg2	2a	0	0	0	0.80(1)	0.10(13)
Na1	2a	0.2119(25)	0	0.5	0.62(1)	1.50(12)
Na2	4b	0.6626(21)	0.16925(7)	0.5	0.62(1)	1.50(12)
O1	2a	0.4095(30)	0	0.1511(9)	1	0.40(26)
O2	2a	0.5982(30)	0	0.7630(13)	1	0.40(26)
O3	4b	0.3832(26)	0.3188(12)	0.1644(10)	1	0.40(26)
O4	4b	0.5955(30)	0.3192(13)	0.8044(11)	1	0.40(26)

Figures

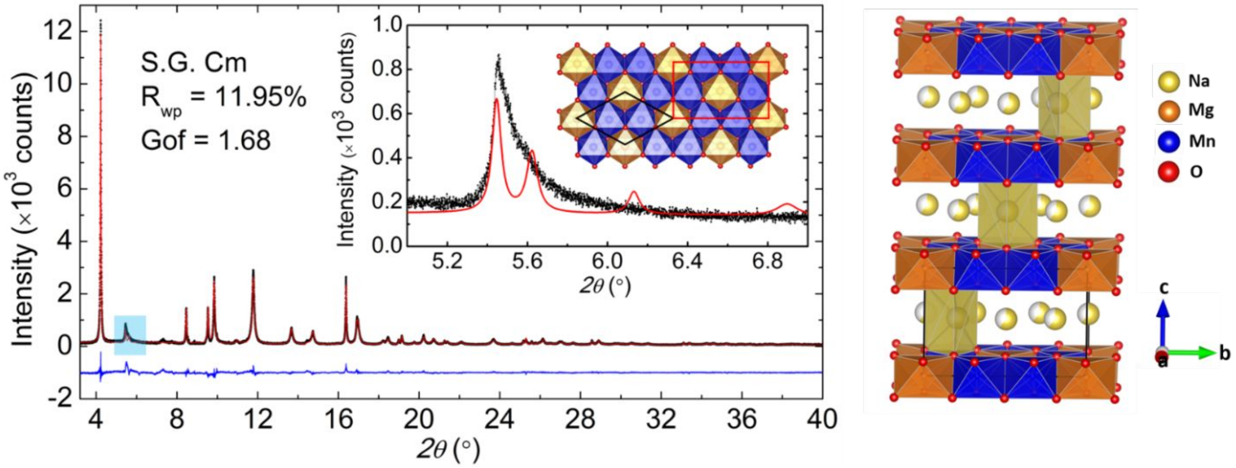

Figure 1. Left, Rietveld refinement of the structure (S.G. *C*m) of $Na_{2/3}Mg_{1/3}Mn_{2/3}O_2$ using synchrotron XRD (λ= 0.412748 Å), insert figure shows the super lattice reflections associated with the in *ab*-plane Mn/Mg honeycomb ordering (with the strong asymmetry due to the stacking disorder of honeycomb ordered layers along the *c*-axis direction). Right, the refined structure of $Na_{2/3}Mg_{1/3}Mn_{2/3}O_2$ (the monoclinic unit cell is shown tripled in the *c*-axis direction).

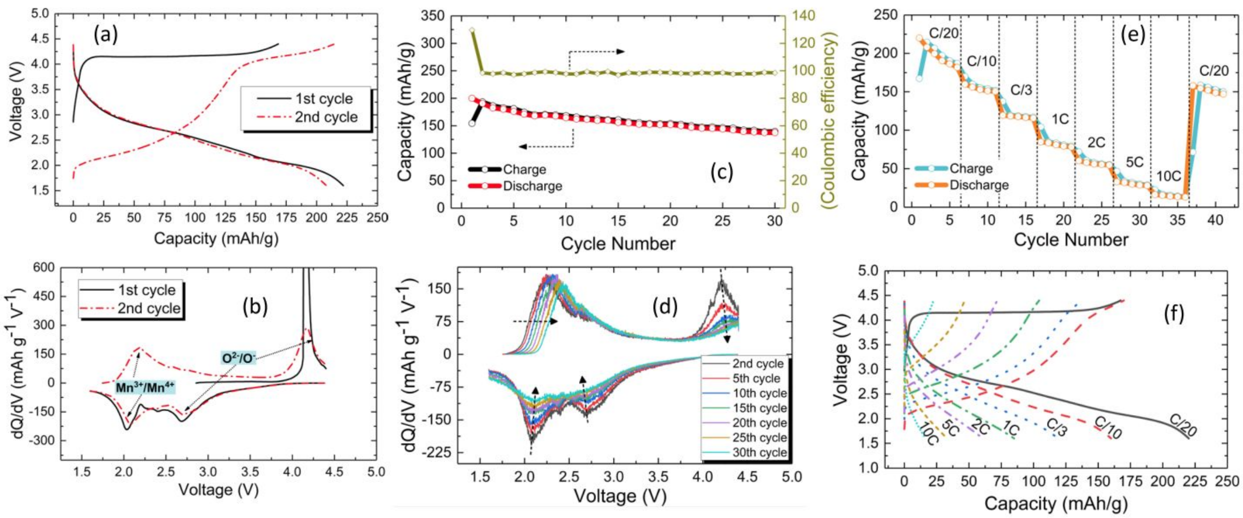

Figure 2. Electrochemistry of P3-type $Na_{2/3}Mg_{1/3}Mn_{2/3}O_2$. (a, b) Charge/discharge curves and corresponding dQ/dV plots for the 1st and 2nd cycle at C/20 between 4.4 and 1.6 V (vs. Na^+/Na). (c, d) Cycle performance at C/10 between 4.4 and 1.6 V and corresponding dQ/dV plots at various cycling stages. (e, f) Rate capability and the initial charge/discharge curves at C/20, C/10, C/3, 1C, 2C, 5C, and 10C between 4.4 and 1.6 V.

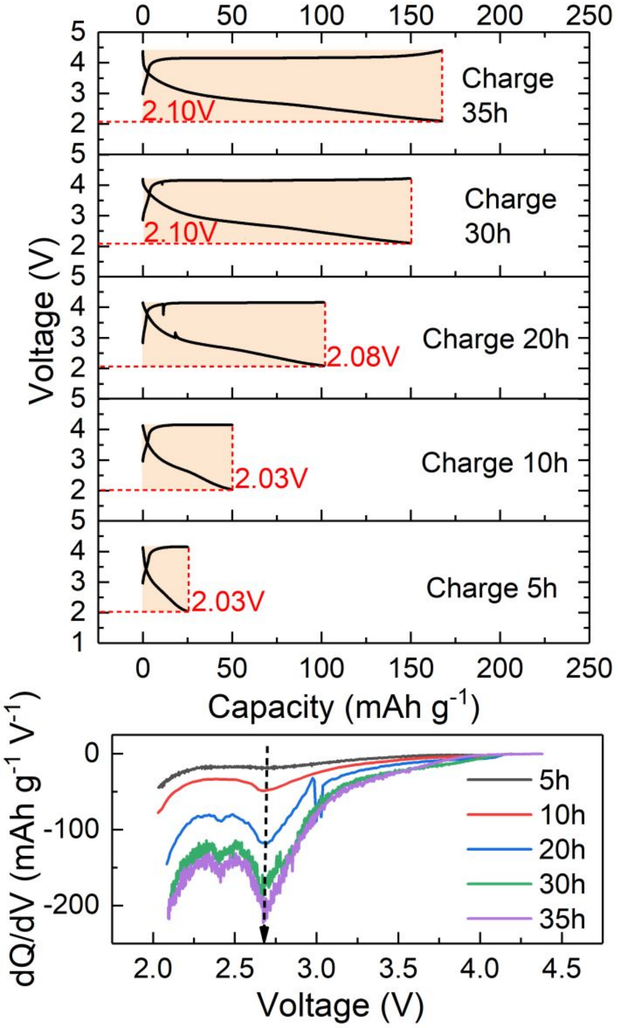

Figure 3. Controlled charge/discharge behaviors of $Na_{2/3}Mg_{1/3}Mn_{2/3}O_2$ at C/20 as a function of charging time, i.e. 5, 10, 20, 30, and 35 h. The discharge curve is cut off to match the same charge capacity at each condition, where the discharge cut-off voltage is marked. The dQ/dV plots for all the discharge curves are also shown for comparison.

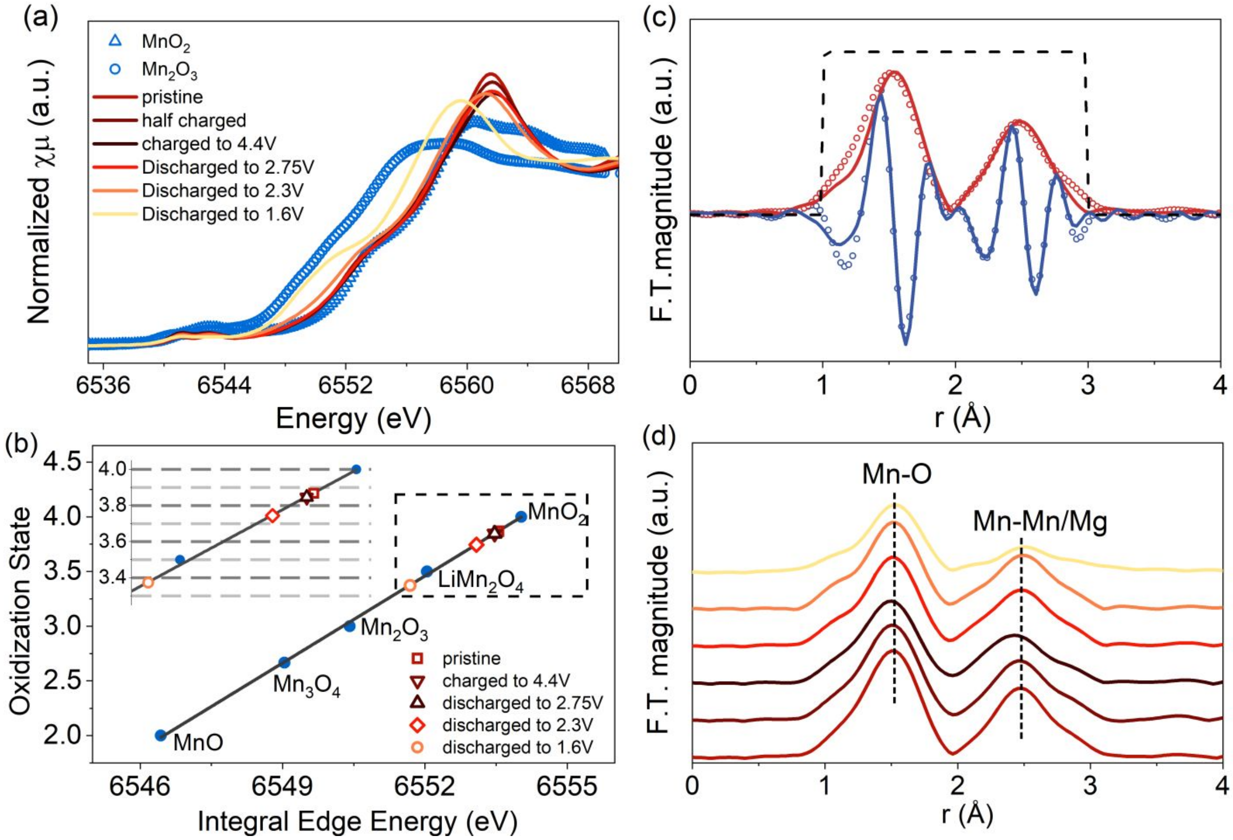

Figure 4. (a) X-ray absorption near edge structure (XANES) of the P3-type $Na_{2/3}Mg_{1/3}Mn_{2/3}O_2$ at various states of charge/discharge with references of Mn_2O_3 and MnO_2 shown. (b) Mn valence at various state of charge determined by using the linear relationship between valence and integral edge energy. (c) Fitting of the Fourier transformed extended X-ray absorption fine structure (EXAFS) of the pristine sample using the structure solved from X-ray diffraction. The blue symbol: the real part of EXAFS; the blue line: the fitted result of the real part; the red symbol: the magnitude of EXAFS; the red line: the fitted result of the magnitude. (d) Fourier transformed EXAFS of P3-type $Na_{2/3}Mg_{1/3}Mn_{2/3}O_2$ at various states of charge. The color code in all panels is the same as that in (a).

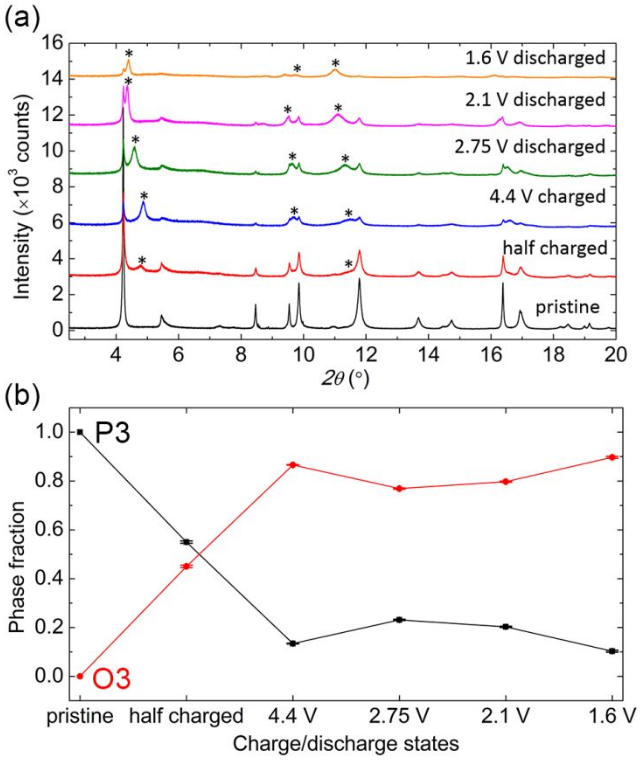

Figure 5. (a) *Ex situ* XRD patterns of P3-type $Na_{2/3}Mg_{1/3}Mn_{2/3}O_2$ at different charge and discharge states. The major reflections associated with O3 phases are marked with stars. More detailed labeling can be found in supporting information Figure S7. (b) Refined (weight-based) phase fraction of the P3 and O3 phases (using Rietveld refinement method) at different charge/discharge states.

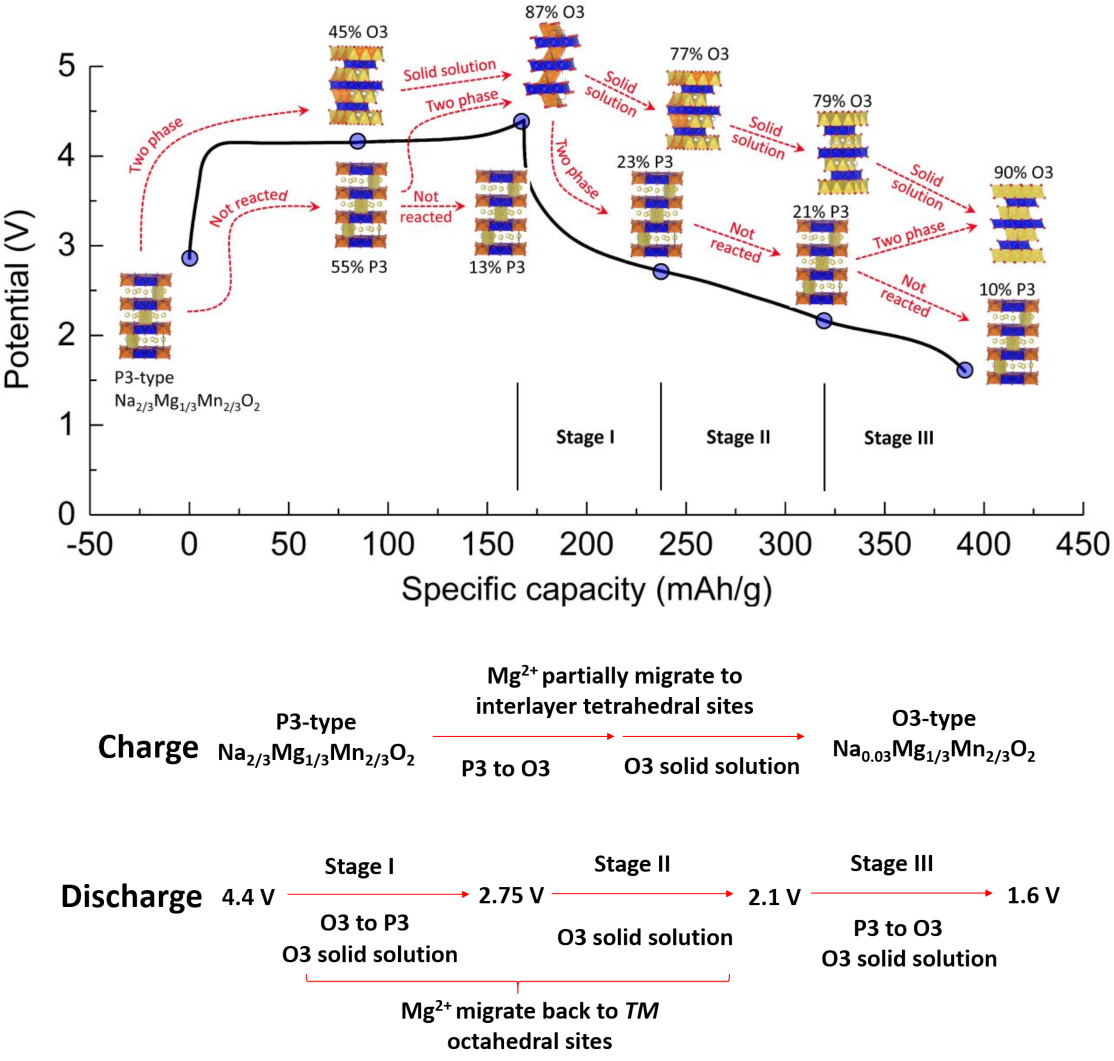

Figure 6. Schematic illustration of the phase transition of the P3-type $Na_{2/3}Mg_{1/3}Mn_{2/3}O_2$ during initial charge and discharge.

Table of Contents Entry

A novel P3-type $Na_{2/3}Mg_{1/3}Mn_{2/3}O_2$ cathode delivers a reversible capacity over 200 mAh/g mainly using lattice oxygen redox.